Aerodynamics in the open channel of the Sistan-type Wind-Mill with Vertical Axis Wind Turbine.

Nomenclature

D	diameter of the wind turbine (m)
$\boldsymbol{f}$	volume force vector
H	half height of the central cavity (m)
k_{r} , k_{s}	ratios $k_{\mathrm{r}} = Q_{x,\mathrm{r}} / Q_{0,\mathrm{r}}$ and $k_{\mathrm{s}} = Q_{x,\mathrm{s}} / Q_{0,\mathrm{s}}$ respectively (%)
n	mesh number (-)
p	pressure (Pa)
p_{r}	relative pressure for the rotating (dynamic) wind turbine (Pa)
p_{s}	relative pressure for the static wind turbine (Pa)
$Q_{x,\mathrm{r}}$, $Q_{x,\mathrm{s}}$	local air mass flow, in dynamic and static modes respectively (kg s^{-1})
$Q_{\mathrm{in,r}}$, $Q_{\mathrm{in,s}}$	inlet air mass flow (x=0), in dynamic and static modes respectively (kg s^{-1})
$Q_{x=0,\mathrm{r}}$	local air mass flow in dynamic modes at $x = 0$ (kg s^{-1})
U_{in}	inlet velocity (m s^{-1})
Re	Reynolds number (-)
$\boldsymbol{U}$	air velocity vector
U_{r} , U_{s}	air velocity in dynamic and static modes respectively (m s^{-1})
$U_{\mathrm{max,r}}$, $U_{\mathrm{max,s}}$	maximum air velocity for the dynamic and static case respectively (m s^{-1})
x, y, z	Cartesian coordinates (m)
z^*	dimensionless coordinate $z^* = z / H$ (-)

Greek symbols

α	angle with respect to the ″Ox″ direction (°)
δ	deviation $\delta = 100\left(U_{\mathrm{max,r}} - U_{\mathrm{max,s}}\right) / U_{\mathrm{max,r}}$ (%)
Δ	deviation $\Delta = 100\left(Q^{i+1}_{x=0,\mathrm{r}} - Q^{i}_{x=0,\mathrm{r}} \middle/ Q^{i}_{x=0,\mathrm{r}}\right)$ between calculation steps (%)

∇^2	Laplacian operator
μ	air dynamic viscosity (Pa s)
ν	air kinematic viscosity ($m^2\ s^{-1}$)
ρ	air density ($kg\ m^{-3}$)

Introduction

Because of the importance of wind energy, many works are devoted to this field. The survey by Bhutta *et al.* (2012) focuses on Vertical Axis Wind Turbines (VAWT) in various conventional configurations: Savonius, Darrieus, combined Savonius-Darrieus and several other configurations such as the Sistan-type windmill, which is considered as one of the oldest machines equipped with a VAWT. The study by Shepherd (1990) presents a comprehensive historical review of windmill development, including the Sistan type. The reader will find in some specialized documents, such as Al-Hassan and Hill (1986), Hau (2006) and Campbell (2011), the technical, technological and architectural aspects of this interesting assembly. Several studies have been done to improve the performance of VAWTs. The work by Altan and Atılgan (2008) is a numerical and experimental survey of a Savonius wind rotor: a wind deflector is installed in front of the rotor in order to reduce the negative-direction torque that occurs on the convex blade of the rotor; the solution is obtained by means of the finite volume method, associated to the Standard k–ε turbulence model with a logarithmic surface function. As concerns the Sistan-type windmills, restoring and operating such machines requires a prior study to clarify some technical characteristics. This is the main objective of the present work that examines the details of the aerodynamic phenomena that occur in one of the best-known version of the Sistan-type wind-mill equipped with a VAWT installed in a channel whose top is open. The proposed CFD approach allows to compensate the absence of experimental data on this historical assembly. The model 3D considered in the present survey reproduces as closely as possible the original assembly. Several inlet velocities are considered, taking into account the local wind resources and its prevailing direction. Calculations are made by means of the finite volume method for Reynolds Numbers varying between $8x10^5$ and $4x10^6$. Turbulence is treated with the realizable k-ε model. The mesh consists of a fixed part connected to the contour of the channel, interfaced with a moving one linked to the turbine equipped with 9 partly-filled wings. The velocity and relative pressure fields are presented for various dynamic and static conditions. Particular attention is paid to the air-mass flow and its

distribution across the channel. This study complements a recent one addressed by Baïri *et al.* (2015) considering the same assembly with a closed top channel.

The treated configuration

The architectural features and other details of the considered assembly are described in several papers presented in the introduction. A general scheme of its operational part is presented in Fig. 1. With 5m height, 7m depth and 18m width, it is constituted of a collector (1), a deflector (2) and a channel containing the Vertical Axis Wind Turbine (3) equipped with 9 plane blades of 5m height and 3m length, numbered from 1 to 9 in Fig. 2 (a). The channel is delimited by the floor and two vertical walls (right (4) and left (5)). Its top is open. The axis of the large turbine is held in place thanks to a crossbar (6). The end of each blade detailed in Fig. 2 (b) is covered on 1m width with a material on which the wind exerts the torque on the turbine axis. The rest of the blade is empty. The origin of the Cartesian reference is centered in the middle of the turbine axis as shown in Fig. 1.

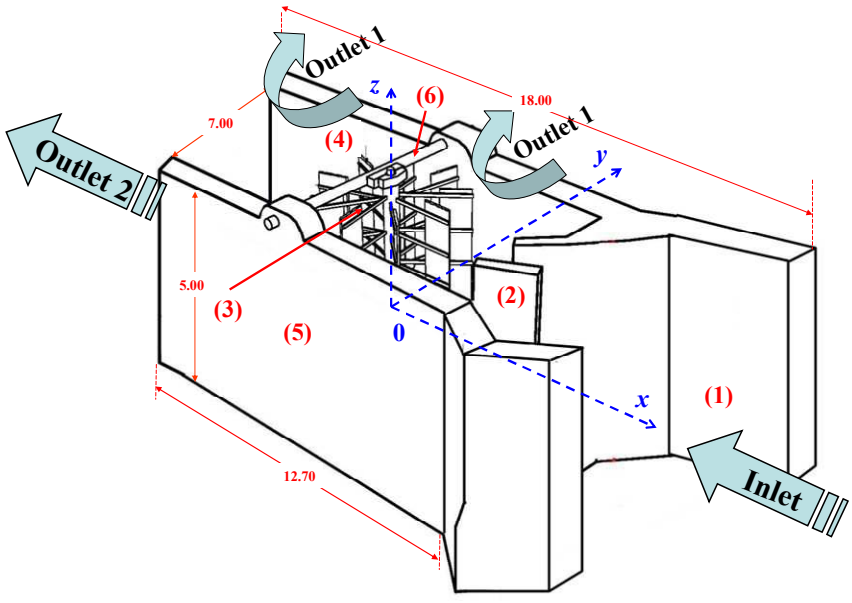

Fig. 1. The treated configuration with open top. All dimensions are in meter (m)

The air enters the channel through the front "*yz*" section (Inlet) and leaves through both the open top section (Outlet 1, "*xy*" section) and the rear section (Outlet 2, "*yz*" section). Some details of the installation are shown in the top view of Fig. (3). The considered

domain is asymmetrical and has large characteristic dimensions. It is oriented in the direction of the prevailing local wind, unlike most traditional VAWTs that can start in any wind direction. Therefore this assembly must be installed only where the prevailing wind direction is clearly known.

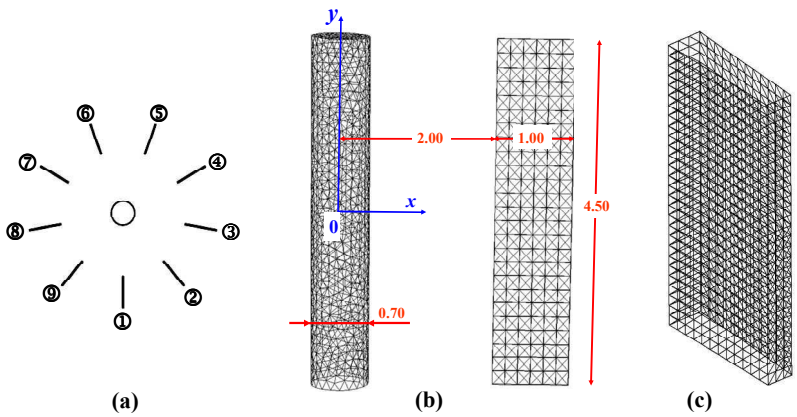

Fig. 2. (a) Numbering blades. **(b)** Details of turbine axis and blade **(c)** Details of the deflector. All dimensions are in meter (m).

Numerical procedure. The adopted mesh

The boundary domain is constituted of 622,239 unstructured triangular elements distributed on the interior faces, including the blades and the axis of the wind turbine. The collector, the deflector, the right and left vertical faces are presented in Fig. 4. The inlet and outlet sections are presented in Fig. 4 in blue and red color respectively.

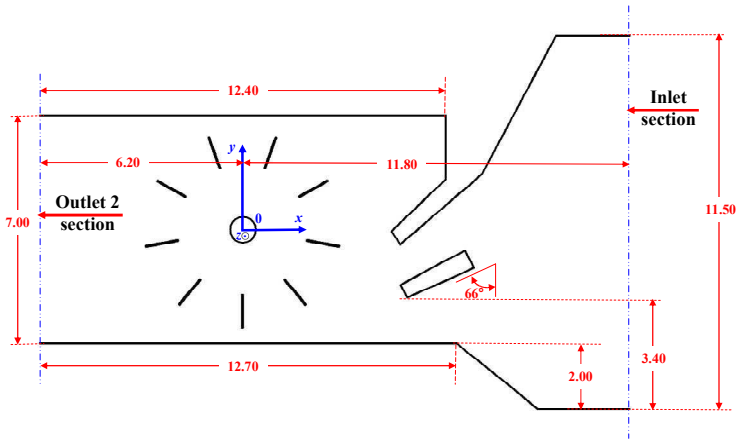

Fig. 3. The considered domain. All dimensions are in **meters** (m).

The velocity distribution is uniform in the Inlet and Outlet 2 sections. This is not the case on the other boundaries subjected to specific aerodynamic phenomena. Details of the floor and the top boundaries (Outlet 1 section) are presented in Fig. 4(c) and 4(d) respectively.

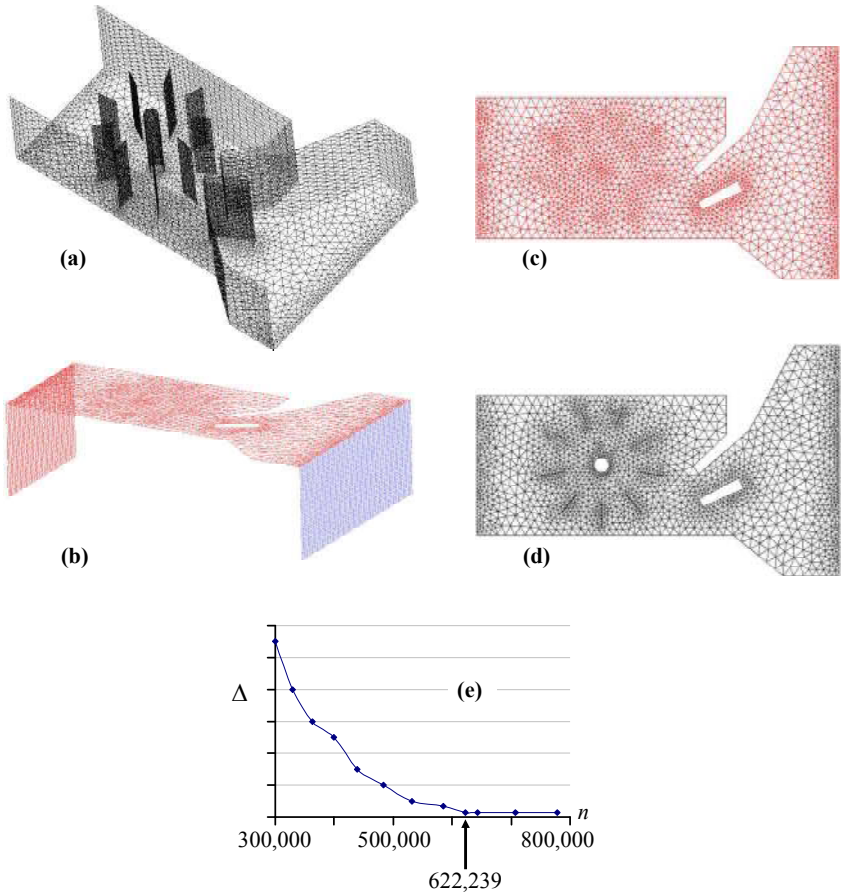

Fig. 4. The adopted mesh **(a)** floor, collector, deflector, right and left vertical walls; **(b)** inlet section (blue color); combined outlet 1 and 2 sections (red color) **(c)** details of the outlet 1 section **(d)** floor details. **(e)** Mesh optimization.

The meshes in the axis and in the blades areas are presented in Fig. 2 (b), and the mesh in the deflector area is presented in Fig. 2(c). The near-wall function has been used to tighten the mesh in the interfaces between the blades and the floor, as well as between the blades and the upper fluid boundary. The concentration function leads to the higher mesh density detailed in Fig. 2 and Fig. 4. The fluid volume consists of 305,188 tetrahedral cells and 56,750 nodes. The mesh is unstructured for easier implementation in the computational domain, given its

complexity and large dimensions. It was adopted after several optimization tests, ensuring a reasonable computing time associated with satisfactory precision. The tests were based on air mass flow balances done at seven $''yz''$ sections numbered from 1 to 7 in the Fig. 5, whose corresponding abscissa are $x=-6.2,-4.0,0.0,+4.0,+6.2,+7.1$ and $+11.8$m respectively. The value of the air mass flow in the central section $(x=0)$ for the dynamic configuration $Q^{i+1}_{x=0,\mathrm{r}}$ is considered to optimize the mesh. The minimum mesh size set at 300,000 elements was increased by 10% at each calculation step i. The mesh is considered optimal and the results as mesh-independent when the air-mass flow values for two consecutive calculation steps do not vary by more than 0.5%, that is to say $\Delta=100\left(Q^{i+1}_{x=0,\mathrm{r}}-Q^{i}_{x=0,\mathrm{r}}/Q^{i}_{x=0,\mathrm{r}}\right)\leq 0.5$. This result is obtained with $n=622{,}239$ elements, as represented in Fig. 4(e).

The angle α referenced with the main flow direction $''Ox''$ (Fig. 5) allows to identify the areas in which particular aerodynamical phenomena may occur.

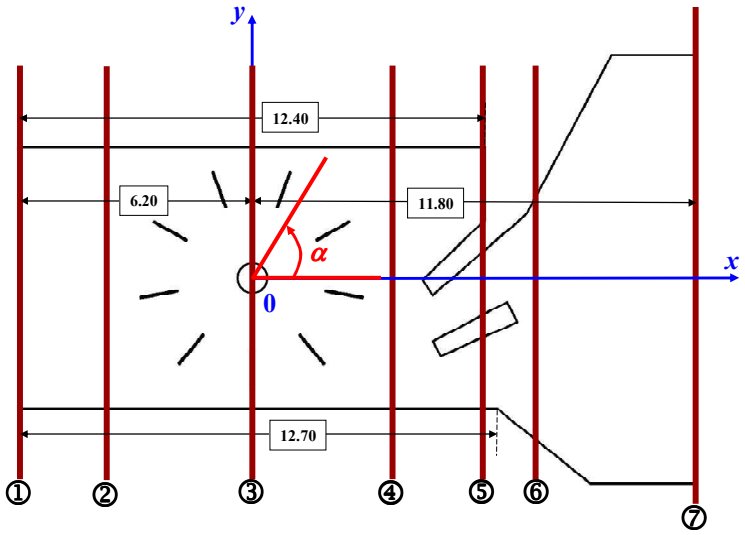

Fig. 5. The $''yz''$ sections for the air mass flow determination. $x=-6.2,-4.0,0.0,+4.0,+6.2,+7.1$ and $+11.8$m for section 1 to 7 respectively. All dimensions are in meter (m)

The phenomena in the boundary layers separation are well identified with the considered mesh. The computational domain is divided into two distinct sub-domains in order to simulated the airflow during the operation of the wind turbine: the rotating volume includes the wind turbine and the fixed sub-domain includes the rest of the computational domain.

They are connected by means of a Sliding Mesh interface. The fluid is assumed to be static at the beginning of the calculating process. The whole assembly remains isothermal (20°C) and at standard atmospheric pressure (10^5 Pa). The air thermal characteristics are kept constant, in particular its dynamic viscosity and density ($\mu = 1.8205 \times 10^{-5}$ Pa s ; $\rho = 1.2047$ kg m^{-3}). Five air inlet velocity values U_{in} are considered in this survey: 2, 4, 6, 8 and 10 ms^{-1}, corresponding to the possible value range in a VAWT installation site.

The Reynolds numbers Re based on the diameter $(D = 6\text{ m})$ of the turbine

$$Re = \frac{U_{in} D}{\nu} \tag{1}$$

varies between 8x10^5 and 4x10^6, corresponding to U_{in} = 2 and 10 m s^{-1} respectively. The mass is set to 1000 kg and the "Oz" component of the mass moment of inertia is set to 10000 kg m². The pressure condition is imposed on Outlets 1 and 2, while the non slip condition is imposed on all internal walls, including the blades. The considered problem cannot be treated in 2D given its asymmetry and complex geometry. Only a 3D approach is able to adequately simulate the corresponding airflows.

The 3D RANS (Reynolds-Averaged Navier Stokes) governing equations

$$\begin{aligned} &\nabla \bullet \boldsymbol{U} = 0 \\ &\rho \frac{\partial \boldsymbol{U}}{\partial t} + \rho(\boldsymbol{U} \bullet \nabla)\boldsymbol{U} = -\nabla p + \mu \nabla^2 \boldsymbol{u} \\ &\frac{\partial \boldsymbol{U}}{\partial t} + (\boldsymbol{U} \bullet \nabla)\boldsymbol{U} = -\frac{1}{\rho}\nabla p + \frac{\mu}{\rho}\nabla^2 \boldsymbol{u} \end{aligned} \tag{2}$$

are solved by means of the Ansys-Fluent software (2011) based on the finite volume method. In these equations, $\boldsymbol{U}$ is the 3D velocity vector and p is the pressure, being ρ and μ the air density and dynamic viscosity respectively. The volume force vector $\boldsymbol{f}$ appears in the second term of the momentum equation $\boldsymbol{f} = (\boldsymbol{U} \bullet \nabla)\boldsymbol{U}$. This system is widely described in several works including those of Anderson (1995) and Versteeg and Malalasekara (1995). The SIMPLE algorithm is adopted for the pressure-velocity coupling in the momentum equations. The time step has been fixed to 50ms and the convergence criteria set to 10^{-4} for both the velocity components and the air-mass flow. Turbulence is treated by means of the realizable

k-ε model which has been implemented in many works such as Walsh and Leong (2004) and Ramsak and Skerget (2008). This model has been choosen because of its easy implementation, good performance and reasonable computing time. This criterion is important in view of the adopted mesh, the large dimensions of the computational domain and the considered Reynolds number values. In addition, the realizable k-ε model is suitable for calculations including rotating fields as is the case in the present work. The reader can find in Altan and Atılgan (2008) and San Martín and Baïri (2014) some details on the turbulence models used in the field of aerodynamics, including the advantages and disadvantages of each one of them depending on the considered application. The results of the realizable k-ε model were compared to those of the RNG model (with 5% turbulence intensity). The mentioned RNG model requires a mesh about 3 times denser on average than the realizable k-ε model, and about 7 times as much calculation time. The deviation in results between these two models is moderate: about 2% on average in air mass flow with a 4% maximum in the 7 considered sections in Fig. 5. These comparisons justify using the realizable k-ε model in the present work.

Results and comments

The velocity and relative pressure fields at $z^* = 0$ are presented in Fig. 6 for the five inlet velocities U_{in} = 2, 4, 6, 8 and 10 ms^{-1}, for both the static and dynamic wind turbine (U_s and U_r respectively). With the assumptions of mass and mass moment of inertia taken into account in this study, the angular velocity of the dynamic wind turbine is 1.393, 2.441, 3.623, 5.015 and 6.665 rd s^{-1} for U_{in} = 2 to 10 ms^{-1} respectively. The general trend of the velocity field is kept for all the considered U_{in} values, in the dynamic and static cases. The maximum velocity, which is specified in each case in Fig. 6, is higher in the dynamic configuration. It is located systematically (i) at the deflector (ii) in the space between blades 1 and 2 and between blades 2 and 3 (iii) on the left vertical wall, adjacent to blade 1 in its downstream area. The deviation $\delta = 100\left(U_{max,r} - U_{max,s}\right)/U_{max,r}$ between the maximum values $U_{max,r}$ and $U_{max,s}$ (dynamic and static turbine, respectively) is presented in Fig. 7. The acceleration is relatively high at low inlet velocities, up to 25% for U_{in} = 2 ms^{-1}. However it decreases with increasing U_{in}, reaching 5.3% for U_{in} = 10 ms^{-1}.

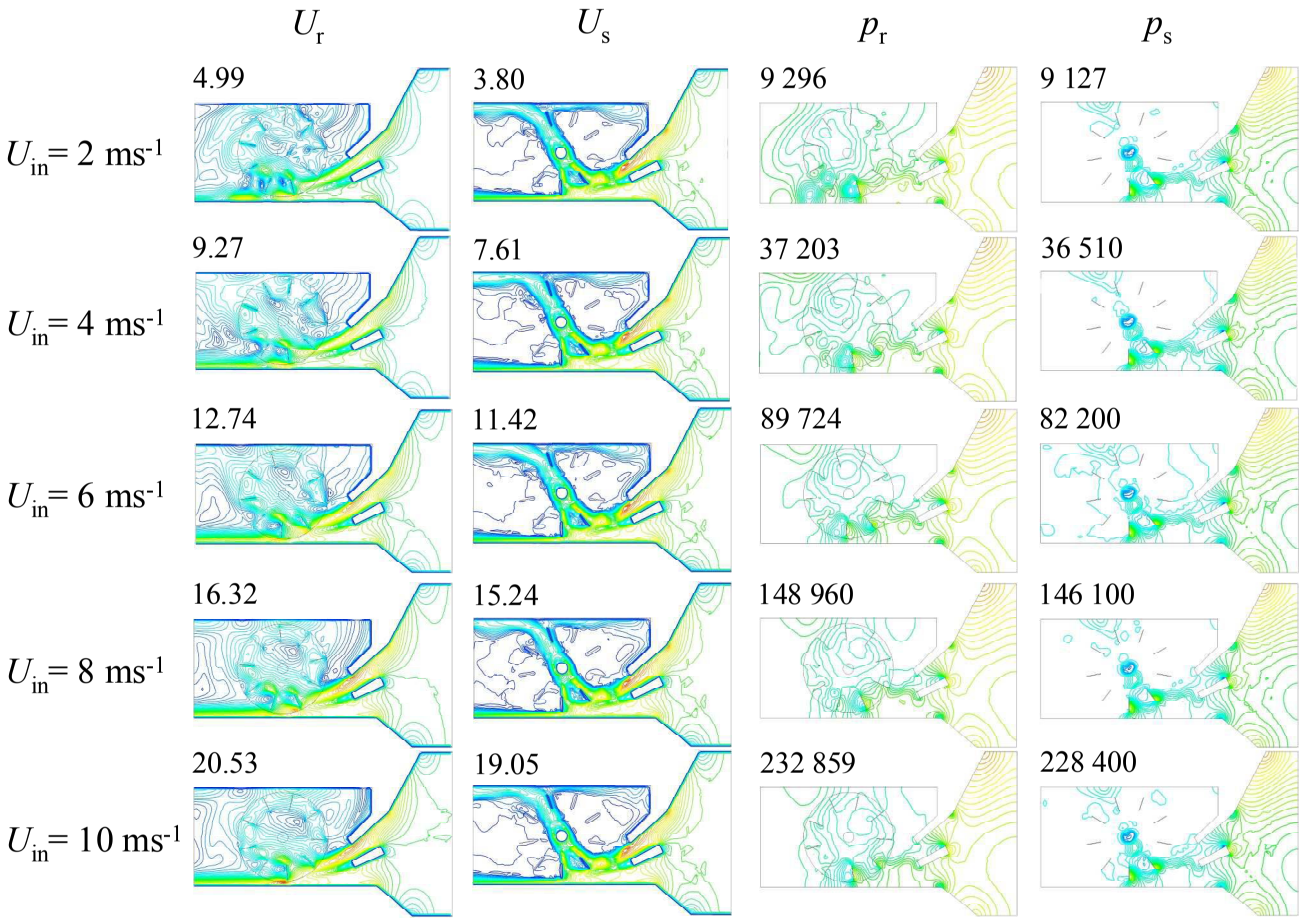

Fig. 6. Velocity and relative pressure fields at $z^* = 0$ for $U_{in} = 2$, 4, 6, 8 and 10 ms^{-1}.

The maximal values (ms^{-1} and Pa) are indicated in both configurations: dynamic (U_r, p_r) and static (U_s, p_s) wind turbine

The rotation of the wind turbine significantly impacts the flow characteristics. The airflow in the volume of the turbine is driven by the rotating blades. The second significant part of the flow is located on the left side of the wall, because of the orientation imposed by the deflector. The remaining volume is characterized by a reduced flow, particularly in the area $(3\text{m} \le x \le 6.2\text{m}\,; 0 \le y \le 3.5\text{m})$. This is confirmed by the low relative pressure values shown in the same figure for all the considered U_{in} values.

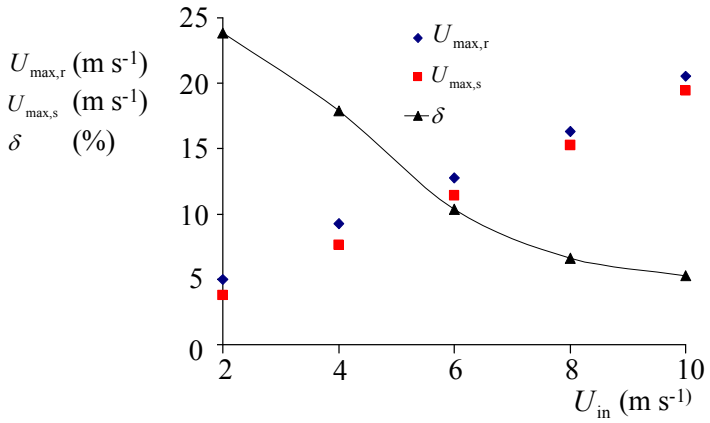

Fig. 7. Maximum velocity airflow $U_{\text{max,r}}$ and $U_{\text{max,s}}$ in the central cavity for the dynamic and static turbine respectively. Deviation δ for $2 \le U_{\text{in}} \le 10\ \text{ms}^{-1}$.

The details presented in Fig. 8(b) for U_{in}=10 ms^{-1} confirm that the forces generated by the flow on the blades generate a positive rotor moment (clockwise rotation) for $180° \le \alpha \le 360°$, and that in $0 \le \alpha \le 180°$ the reversal flow is not intense enough to counterbalance the positive moment. Furthermore, it has to be noted that one or more vortices may develop in the domain. Depending on their location, intensity and direction of rotation, these aerodynamic phenomena could disturb the rotation of the wind turbine and degrade its performance. This aspect was of course examined for all the treated cases. For U_{in}=10 ms^{-1} presented in Fig. 8(a), a stationary vortex is located within the area surrounding the turbine, at $\alpha \approx 30°$. This vortex is of low intensity (low velocity vectors) and is in the same rotating direction as the wind turbine (clockwise), which does not disturb its operation. For U_{in}=2 ms^{-1} presented in Fig. 8(c), a vortex is located outside the volume enclosing the turbine. It contributes to a slight improvement of the aerodynamic performance of the turbine given the

direction and intensity of the velocity vectors. This phenomenon appears in the other inlet velocity cases too. In all cases, the aerodynamic performance of the turbine is not affected.

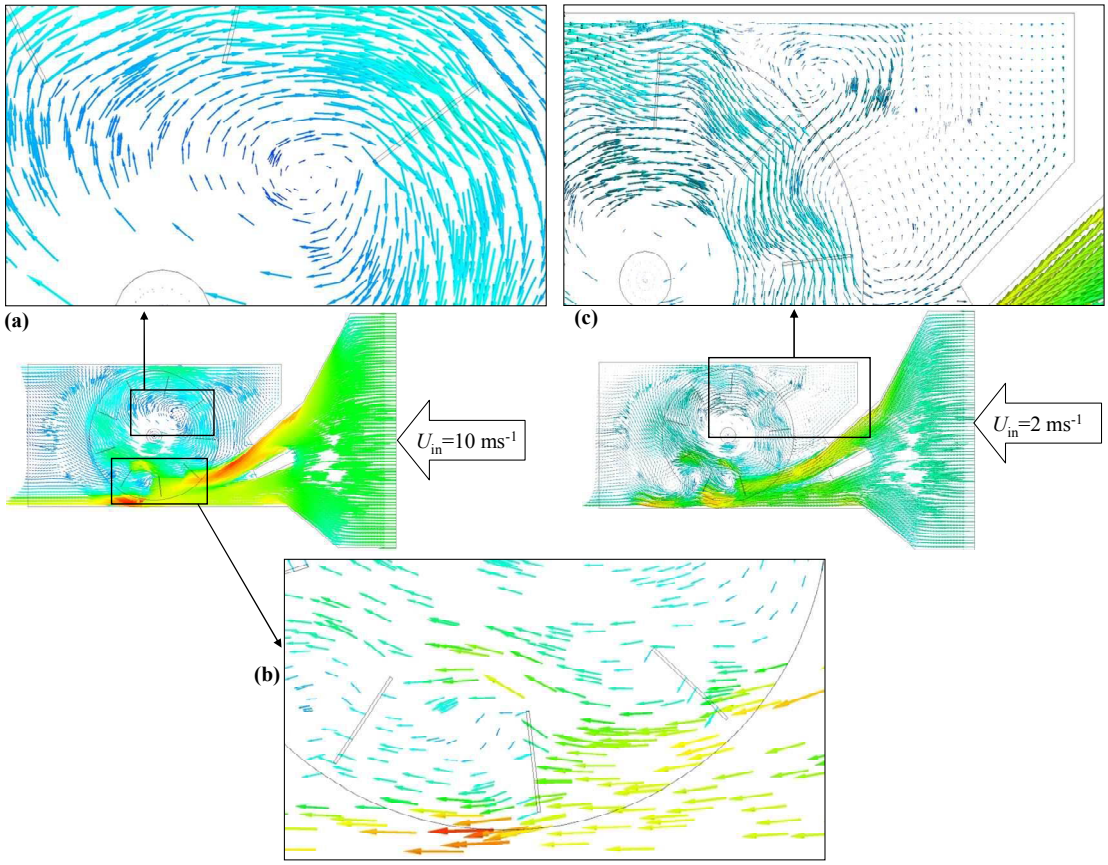

Fig. 8. Dynamic wind turbine: Details of **(a)** the vortex for U_{in}=10 ms^{-1} **(b)** the flow on the blades 1, 2 and 9 **(c)** the vortex for U_{in}=2 ms^{-1}.

When the turbine is stopped, the flow in the central cavity is divided into two main directions: (i) near the left wall, due to the deflection angle, (ii) through the uncovered part of the blades, at an angle $\alpha \approx 120°$. This is the case for all treated U_{in} values, as represented in Fig. 9 for U_{in}=10 ms^{-1}. In this static configuration, a large part of the air mass flow is oriented towards the vertical right wall. Two zones are characterized by a very feeble flow: the first one is located in the same area as in the dynamic wind turbine configuration, and the second one is located behind the wind turbine towards outlet 2. The relative pressure distributions confirm that the air flow is of low intensity in both areas.

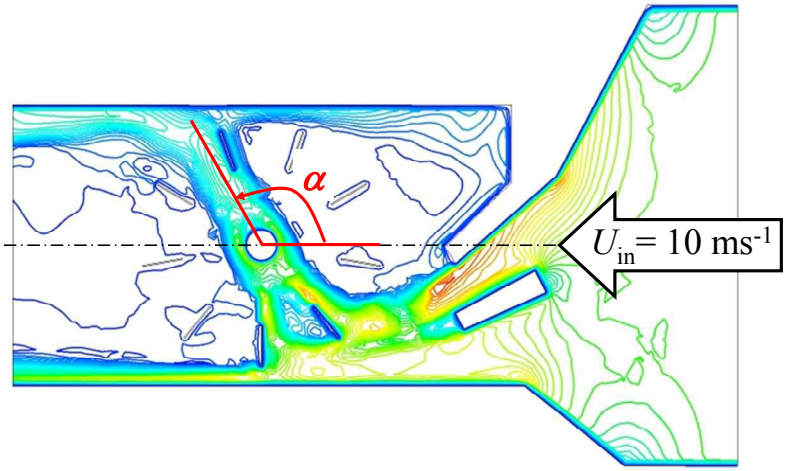

Fig. 9. The two main airflow directions in the static wind turbine. U_{in}=10 ms^{-1}

The evolution of the air mass flow in the dynamic case $Q_{x,r}$ is presented in Fig. 10 at sections 1 to 6 for U_{in}=10 ms^{-1}. The air mass flow balance was systematically computed along the main direction $"x"$. The adopted convergence criteria provide a maximum deviation of about 0.2% on average, which is considered to be satisfactory.

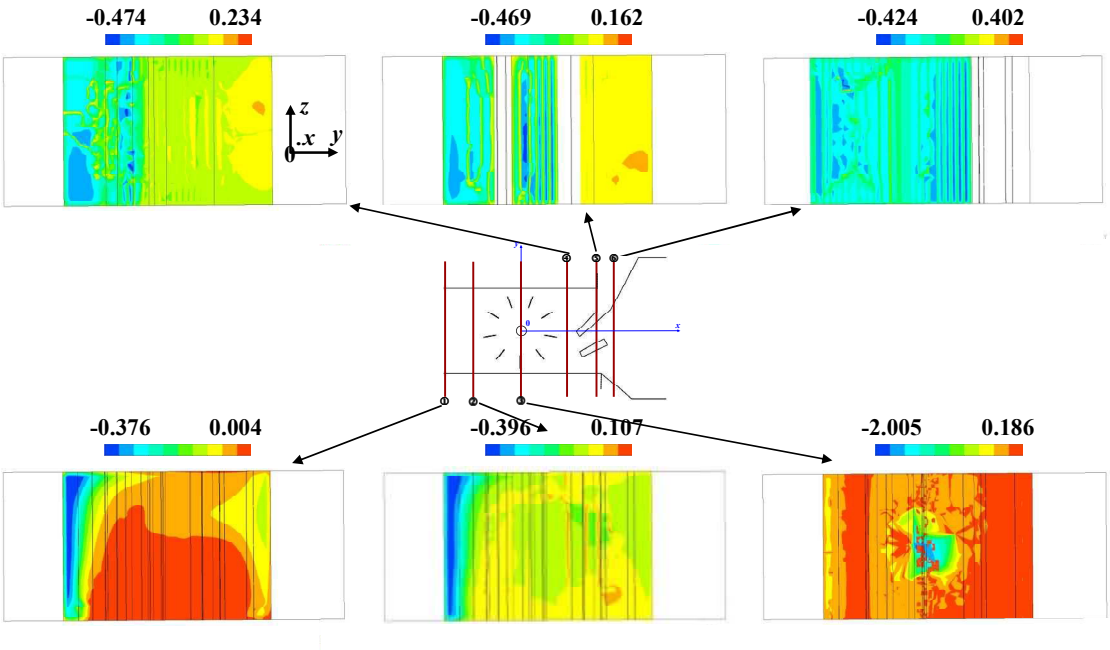

Fig. 10. Evolution of the air mass flow $Q_{x,r}$ at sections 1 to 6 for the dynamic wind turbine and U_{in}=10 ms^{-1}

The air mass flow is presented in Fig. 11(a) and (b) in the dynamic and static configurations respectively. The trends are the same, but the values are systematically higher in the dynamic configuration. The air mass flow for a given abscissa x corresponding to sections 1 to 6 is denoted by $Q_{x,\mathrm{r}}$ and $Q_{x,\mathrm{s}}$ in the dynamic and static configurations respectively. The ratios

$$k_\mathrm{r} = Q_{x,\mathrm{r}} / Q_{\mathrm{in,d}} \; ; \; k_\mathrm{s} = Q_{x,\mathrm{s}} / Q_{\mathrm{in,s}} \tag{3}$$

are presented in Fig. 11(c), being $Q_{\mathrm{in,r}}$ and $Q_{\mathrm{in,s}}$ the air mass flow across section 7 (inlet). For a given section, this ratio remains constant (at ±0.5%) for the considered U_in, in both static and dynamic configurations.

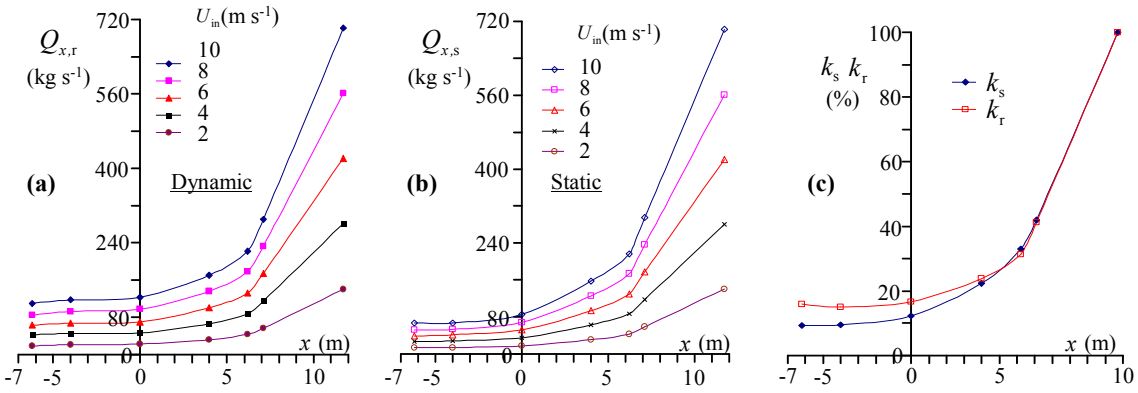

Fig. 11. Evolution of the air mass flow at sections 1 to 7 for the turbine **(a)** dynamic **(b)** static. **(c)** Evolution of k_r and k_s . U_in = 2, 4, 6, 8 et 10 ms^{-1}

As compared to section 7 (inlet), the air mass flow is significantly reduced on section 6, which is where the air mass effectively enters the active part of the assembly. Only 42% of the mass admitted in section 7 penetrates into the cavity. This portion is nevertheless characterized by a higher momentum due to the effects of the collector located upstream. The average velocity substantially increases when flowing through section 5, where the deflector is located. The portion that is extracted through the top of the cavity (outlet 1) when air flows through the central cavity is about 26% and 33% of the mass admitted through section 7, in dynamic and static configurations respectively. However, when comparing to the air mass effectively admitted into the cavity (section 6), it appears that most of the air mass is extracted

through the top of the cavity: about 61% in the dynamic configuration and 78% in the static one.

Conclusion

This work examines the aerodynamic phenomena occurring in one of the best-known versions of the Sistan-type windmill. This assembly is equipped with a Vertical Axis Wind Turbine installed in a channel with an open top. This survey complements a previous one examining the aerodynamical phenomena occurring in a modified version of this assembly with a closed top channel. The numerical approach is carried out by means of the finite volume method with a 3D model reproducing as closely as possible the original assembly. Calculations are done by using the Sliding Mesh interface technique. Various inlet velocities are considered, based on the possible local wind resources implying Reynolds Numbers varying between $8x10^5$ and $4x10^6$. The velocity and relative pressure fields are presented in various dynamic and static configurations. Particular attention is devoted to the air mass flow and its distribution between the inlet and outlet sections of the channel. Calculation results clearly show that the vortex phenomena that occur in some cases cannot be a source of degradation of the wind turbine's aerodynamical performance, given its location, intensity and rotation direction. The technical results of this work could be used for the restoration and operation of this assembly whose historical and architectural relevancy is recognized.

References

Al-Hassan A.Y. and Hill, D.R. (1986) "Islamic technology: an illustrated history", Cambridge Press, Cambridge University.

Almohammadi, K.M., Ingham, D.B., Ma, L. and Pourkashan, M. (2013) "Computational fluid dynamics (CFD) mesh independency techniques for a straight blade vertical axis wind turbine", *Energy* Vol. 58 pp. 483-493.

Altan, B.D. and Atılgan, M. (2008) "An experimental and numerical study on the improvement of the performance of Savonius wind rotor", *Energy Conversion and Management* Vol. 49 pp. 3425–3432.

Anderson, J.D. (1995) "Computational Fluid Dynamics: The Basics with Applications", 6th ed., McGraw Hill, ISBN: 0070016852, 1995.

ANSYS, CFX v14 (2011), Help Manuals, Solver Theory, http://dx.doi.org/www.ansys.com/cfx.

Baïri, A., Crua, C., Bauzin, J.G. and Baïri, I. (2015) "Aerodynamical phenomena in a large top covered wind mill with vertical axis wind turbine", *International Journal of Numerical Methods for Heat & Fluid Flow*, accepted manuscript, under press.

Bhutta, M.M.A., Hayat, N., Farooq, A.U., Ali, Z., Jamil, S.R. and Hussain, Z. (2012) "Vertical axis wind turbine. A review of various configurations and design techniques", *Renewable and Sustainable Energy Reviews* Vol. 16 pp. 1926–1939.

Campbell, J.L. (2011) "Architecture and Identity: The occupation, use, and reuse of Mughal Caravanserais", PhD thesis, Department of Anthropology, University of Toronto.

Hau, E. (2006) "Wind turbines–fundamentals, technologies, application, economics" 2nd ed. Berlin, Heidelberg: Springer-Verlag.

Ramsak, M. and Skerget, L. (2008) "Boundary element method for thermal flows using *k*-ε turbulence models", *International Journal of Numerical Methods for Heat & Fluid Flow* Vol. 18 No. 3/4 pp. 514-532.

San Martín, D. and Baïri, A., (2014) "Review of the mains turbulence models used in thermal and aerodynamical problems", LTIE-GTE Internal report 025.1-14, 2014.

Shepherd, D.G. (1990) "Historical development of the windmill", NASA contractor report 4337, DOE/NASA/5266-1.

Versteeg, H.K. and Malalasekara, W. (1995) "An introduction to computational fluid dynamics. The finite volume method", ISBN 0-582-21884-5, Pearson Education Limited, 1995.

Walsh, P.C. and W.H. Leong (2004) "Effectiveness of several turbulence models in natural convection" *International Journal of Numerical Methods for Heat & Fluid Flow* Vol. 14 No. 5 pp. 633-648.